Design of TiVNb-(Cr, Ni or Co) multicomponent alloys with the same valence electron concentration for hydrogen storage

Bruno Hessel Silva, Claudia Zlotea, Walter José Botta, Yannick Champion, Walter José Botta, Guilherme Zepon

Design of TiVNb-(Cr, Ni or Co) multicomponent alloys with the same valence electron concentration for hydrogen storage.

Bruno Hessel Silva[a], Claudia Zlotea[b,#], Yannick Champion[c], Walter José Botta[a,d], Guilherme Zepon[a,d,#]

a - Federal University of São Carlos, Graduate Program in Materials Science and Engineering, Federal University of São Carlos (PPGCEM/UFSCar) - Rodovia Washington Luiz, km 235, São Carlos – São Paulo, Brasil CEP:13565-905.

b - Univ Paris Est Créteil, CNRS, ICMPE, UMR 7182, 2 Rue Henri Dunant, 94320, Thiais, France.

c - Univ. Grenoble Alpes, CNRS, SIMaP, 38000 Grenoble, France.

d - Federal University of São Carlos, Department of Materials Engineering (DEMa/UFSCar) - Rodovia Washington Luiz, km 235, São Carlos – São Paulo, Brasil CEP:13565-905.

 # Corresponding authors: zepon@ufscar.br ; claudia.zlotea@icmpe.cnrs.fr

Abstract

Recently, it has been hypothesized that the hydrogen sorption properties of body-centered cubic (BCC) multicomponent alloys might be related to the alloy's valence electron concentration (VEC). In this work, we employed CALPHAD method to design three BCC alloys with the VEC to evaluate this hypothesis. The $(TiVNb)_{85}Cr_{15}$, $(TiVNb)_{95.3}Co_{4.7}$ and $(TiVNb)_{96.2}Ni_{3.8}$ multicomponent alloys with VEC = 4.87 were produced by arc melting. Although some amount of segregation could not be avoided, the as-cast microstructures were composed of a BCC phase with highly homogeneous chemical composition. The alloys quickly absorb hydrogen at room temperature and formed FCC hydrides with high capacities of 2 H/M (3.1-3.2 wt.%). For the three alloys, it was observed a two-step hydrogenation sequence indicating the formation of an intermediate BCC monohydride prior to the formation of the FCC dihydride. Moreover, the three alloys presented very similar values of enthalpy and entropy of hydrogenation, showing that the initial hypothesis seems to hold for the thermodynamic properties. The alloys hydrogenation/dehydrogenation cycling behavior were also evaluated. $(TiVNb)_{85}Cr_{15}$ had a small and continuous drop in capacity over cycling that was addressed to incomplete transformation of the BCC monohydride to the FCC dihydride, whereas $(TiVNb)_{95.3}Co_{4.7}$ and $(TiVNb)_{96.2}Ni_{3.8}$ showed a more stable behavior achieving a reversible capacity of 1.76 H/M (2.77 wt.%) after 20 cycles. The desorption is strongly affected by absorption/desorption cycling for all alloys, as revealed by thermo desorption spectroscopy (TDS). The onset

temperature of desorption depends on the alloys' composition as well as the number of hydrogenation/dehydrogenation cycles. The results suggest that cycling and desorption properties of the alloys are less related to their VEC.

Keywords: Hydrogen storage; Multicomponent alloys; Cycling stability; BCC alloys.

1. Introduction

Hydrogen as an energy carrier has great potential to change the current energy matrix system due to its high calorific energy, environmental-friendly advantages and relatively simple production [1,2]. Among the main barriers of implementing hydrogen in energy applications, the storage method is one of the keys to reach a more efficient, safe and cost-effective solution [3–8]. However, intrinsic properties of hydrogen as the very low boiling point (20.4 K at 1 atm), the low density in gaseous state (90g/m^3) and its flammability make its storage for different applications very challenging [4]. Storage methods have been discussed and compared in terms of different factors as volumetric/gravimetric capacity, reversibility, heat exchange, cost and other technological parameters [5,7,9]. Solid-state storage through metal hydrides is a safe and compact option that has the potential to outperform physical methods as compressed hydrogen tanks and cryogenic storage. However, the great variety of alloy and hydride compositions to be assessed demand a substantial research effort [3,4,8].

Recently, novel groups of alloys known as high entropy alloys (HEA), complex concentrated alloys (CCA), multi-principal element alloys (MPEA) or more generically multicomponent alloys were introduced by the scientific community, expanding the options of compositions to be assessed [10]. Differently from conventional alloys, these groups are based on at least 3 elements having substantial atomic fraction, i.e., alloys belonging to the central part of multicomponent phase diagrams. Such multicomponent alloys can either form single solid solutions with simple structures, such as face-centered cubic (FCC), body-centered cubic (BCC) and hexagonal close-packed (HCP), or more complex structures combining multicomponent solid solutions and intermetallic compounds [10]. Most of the works reported so far present the mechanical and functional properties of single-phase alloys. However, there is still a reduced number of studies in the literature regarding hydrogen storage properties [11–25]. Despite this, interesting hydrogen storage behavior have been recently described for different multicomponent alloys. For example, Sahlberg et al. [11] claimed a superior hydrogen absorption capacity in the TiVZrNbHf alloy. This alloy has a BCC structure and upon

hydrogenation forms a BCT hydride with capacity of up to 2.5 H atom per metal atom ratio (H/*M*), which is higher than the maximum ratio of typical transition metal hydrides (H/*M*=2). Such behavior was linked to the lattice strain, which according to the authors favors hydrogen occupancy in both tetrahedral and octahedral interstitial sites resulting in a body centered tetragonal (BCT) structure in the full hydride phase. Nygard et al. [22] investigated hydrogen storage properties in high-entropy alloys with varying degree of local lattice strain but no correlation between hydrogen storage capacity and the local lattice strain was observed. In a subsequent work, Zlotea et al. [19] described hydrogen sorption in the BCC TiZrNbHfTa alloy. The hydrogenation of this alloy takes place in a two-step phase transformation: first the BCC phase transforms to a monohydride with BCT structure and, subsequently, the BCT monohydride forms a FCC dihydride. In another research line, Zepon et al. [18] reported a hydrogen-induced phase transition in the BCC $MgZrTiFe_{0.5}Co_{0.5}Ni_{0.5}$ alloy produced by high energy ball milling. Under 2 MPa of hydrogen and 350 ºC, this alloy presented a hydrogen uptake of 1.2 wt.% (H/M=0.68). During absorption, a FCC hydride is formed but only a fraction of the BCC phase was converted to FCC. Edalati et al. [25] in a different approach, produced TiZrCrMnFeNi with 95 wt.% of C14 and 5% BCC phases and showed a reversible hydrogenation process (3 cycles) at room temperature, in which the alloy absorbed/desorbed 1 H/M (1.7 wt.%).

Due to the vast range of compositions and multiple possible systems to be evaluated, different strategies have been proposed to find potential alloys with good hydrogen sorption properties. These strategies include the use of CALPHAD method to predict compositions that form single-phase alloys [25], the use of computational modelling based on density functional theory (DFT) [26] and the analysis of empirical/intrinsic alloys parameters in the hydrogen absorption properties, for example, the effect of the lattice strain caused by the atomic size mismatch between the alloy's elements [22]. Recently, Nygard et al. [21] suggests that hydrogen sorption properties in BCC multicomponent alloys might be related to the valence electron concentration (VEC), defined by equation (1).

$$VEC = \sum_{i=1}^{N} \{c_i (VEC)_i\} \quad (1)$$

where c_i is the atomic fraction of each element i with valence-electron concentration $(VEC)_i$ in a multicomponent alloy with N different elements. According to the authors this parameter could be used for tunning the alloy's hydrogen storage properties. It was observed a

trend based on the results of hydrogen capacity of a few high entropy alloys, where the alloys with VEC < 4.75 reached maximum capacity of 2 H/M, whereas alloys with VEC > 5 presented reduced maximum capacity (meaning H/M < 2.0). In addition to these observations, they also reported that the FCC hydrides formed from alloys with VEC > 4.75 presented spontaneous desorption of hydrogen when removed from the high-pressure environment. These remarks indicated that producing alloys with VEC in a range of 4.75-5 might result in materials with high hydrogen capacity and good reversibility at room temperature, which are important requirements for industrial applications. Moreover, the equimolar alloy TiVNbCr studied by Nygard et al. [21] with VEC = 5 showed a reversible hydrogen storage capacity of 1.96 wt.% at room temperature and moderate pressures and did not depend on any activation procedure.

In the present work, CALPHAD method was employed for designing three BCC multicomponent alloys, namely $(TiVNb)_{85}Cr_{15}$, $(TiVNb)_{95.3}Co_{4.7}$ and $(TiVNb)_{96.2}Ni_{3.8}$, with the same VEC = 4.87. The three alloys were produced by arc melting and the hydrogen storage properties in terms of hydrogen capacity, kinetics of absorption, thermodynamic properties of hydride formation and desorption, cycling reversibility, and temperature of desorption were evaluated.

2. Material and methods

2.1 Alloy designing and synthesis

CALPHAD method using Thermo-Calc® software and TCHEA3 database was employed to design three BCC alloys with the same VEC. The equiatomic TiVNb system was used as base material and different amounts of Cr, Co or Ni were added aiming the formation of single BCC solid solutions with the same VEC. The $(TiVNb)_{85}Cr_{15}$, $(TiVNb)_{95.3}Co_{4.7}$ and $(TiVNb)_{96.2}Ni_{3.8}$ alloys were then chosen, satisfying the crystal structure criteria and VEC = 4.87. The alloys were synthesized by electric arc melting under argon atmosphere using pieces of Ti (Goodfellow, 99.8% metals basis), Nb (Goodfellow, 99.8% metals basis), V (Goodfellow, 99.7% metals basis), Cr (Goodfellow, 99.9% metals basis), Co (Goodfellow, 99.5% metals basis) and Ni (Goodfellow, 99.9% metals basis) as feedstock material. Ti-getter pieces were melted prior to alloy's production to minimize oxygen content in the samples. The alloys were produced by melting initially only Ti and Nb pieces to form a binary alloy. Subsequently, the remaining elements were added and melted to obtain the desired alloys – this procedure was adopted to avoid incomplete fusion of Nb pieces. To ensure chemical homogenization, the ingots were remelted five times, with the ingots being turned upside down before each remelt

procedure. Moreover, the alloys were stored in a Mbraun glovebox under argon atmosphere with levels of O_2 and H_2O lower than 0.5 ppm.

2.2 Sieverts measurements

To perform hydrogen sorption experiments, small pieces of the alloys (cut using a manual shear cutter) were loaded into a Sieverts-type apparatus. Before each experiment, the samples were subjected to a heat treatment at 390 ºC under dynamic vacuum for 12 hours (activation procedure to facilitate hydrogen absorption). The samples were then cooled to room temperature and exposed to hydrogen at 25-30 bar for hydrogen absorption kinetic measurements. PCI measurements were carried out at RT and three other temperatures between 100 ºC and 200 ºC to evaluate plateau enthalpy and entropy using Van't Hoff equation (equation (2)). The PCI curves were obtained in absorption and desorption conditions applying variable doses of hydrogen up to the maximum pressure of 100 bar. For cycling experiments, the absorption was carried out under hydrogen pressures of 22-28 bar for three hours and the desorption consisted in heating up the sample to 390 ºC under dynamic vacuum for 12 hours. The alloys were subjected to twenty cycles of hydrogen absorption and desorption without air exposure.

$$\frac{1}{2}\ln\left(\frac{P_{eq}}{P^o}\right) = \frac{\Delta H}{RT} - \frac{\Delta S}{R} \quad (2)$$

2.3 Structure characterization

X-ray diffraction (XRD) were performed using a D8 Advance Brucker diffractometer with Cu-Kα radiation. Phase structure identification and Rietveld refinement analysis were carried out using the software General Structure Analysis System II (GSAS-II) [27]. The microstructure of the alloys in the as-cast condition was assessed by Scanning Electron Microscopy analysis (SEM) acquiring back-scattered electron signal (BSE) using a Zeiss Merlin microscope. Qualitative and quantitative chemical composition were evaluated by energy dispersive X-ray spectroscopy (EDS). The data was acquired using an acceleration voltage of 20 kV, beam current of 5 nA at a working distance of 10 mm. Prior to SEM and EDS analysis, samples were embedded into resin, grinded with SiC papers with mesh sizes of 180, 320, 600 and 1200 followed by polishing in 3 µm, 1 µm and 0.25 µm diamond suspensions.

2.4 Thermo desorption analysis

The desorption properties were analyzed by Thermo Desorption Spectroscopy (TDS). The experiments were done in a homemade apparatus equipped with a quadrupole mass spectrometer which recorded partial pressures of H_2 during the desorption experiments. Moreover, the equipment was attached to a secondary vacuum pump, which provided vacuum pressures of 10^{-6} mbar. For the TDS tests, 10-15 mg of each hydrogenated sample were inserted in aluminum crucibles and then heated at 5 ºC/min up to 450 ºC.

3. Results and Discussion

3.1 Alloy Design and Structural Characterization.

Figures 1 (a), (b) and (c) show the calculated amount of equilibrium phases as function of temperature for $(TiVNb)_{85}Cr_{15}$, $(TiVNb)_{95.3}Co_{4.7}$ and $(TiVNb)_{96.2}Ni_{3.8}$, respectively. The thermodynamic calculation suggests that under equilibrium conditions the $(TiVNb)_{85}Cr_{15}$ and $(TiVNb)_{96.2}Ni_{3.8}$ solidify as single BCC solid solutions. On the other hand, the $(TiVNb)_{95.3}Co_{4.7}$ alloy solidifies as 98 % BCC solid solution and 2% as B2 ordered phase at 1090 ºC. The composition of both BCC solid solution and B2 phase at 1090 ºC are presented in Table 1. One can see that even if a small fraction of the B2 phase was formed, the BCC phase would still have a chemical composition close to the nominal one.

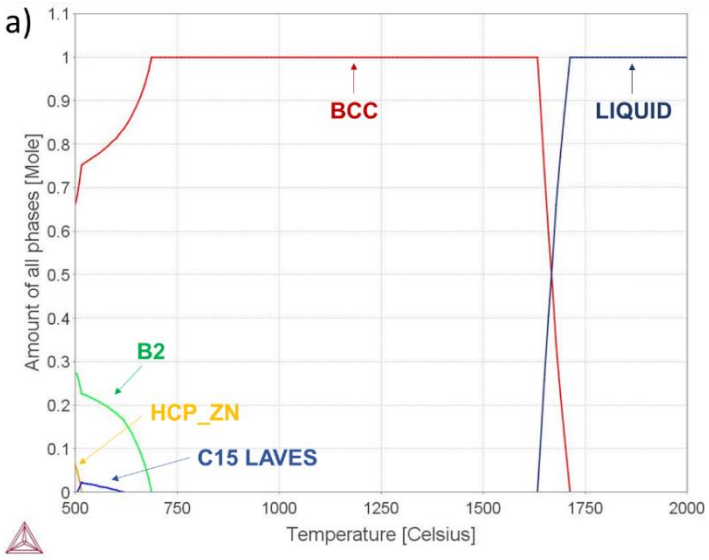
a)
BCC
LIQUID
B2
HCP_ZN
C15 LAVES
Amount of all phases [Mole]
Temperature [Celsius]

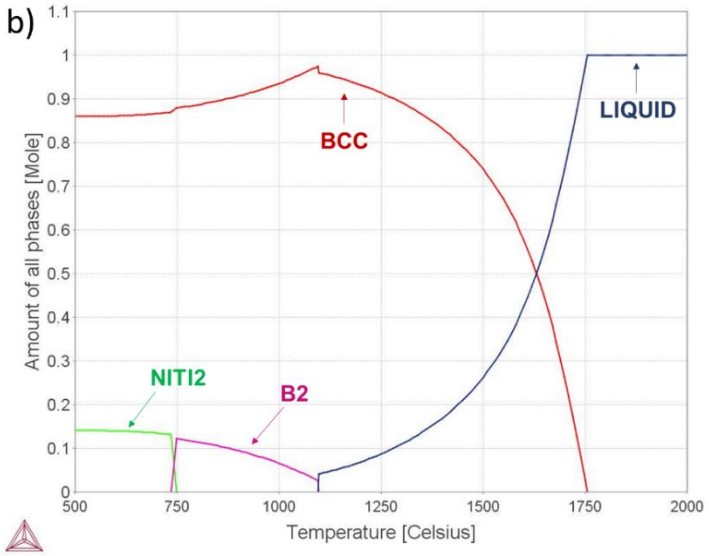
b)
BCC
LIQUID
NITI2
B2
Amount of all phases [Mole]
Temperature [Celsius]

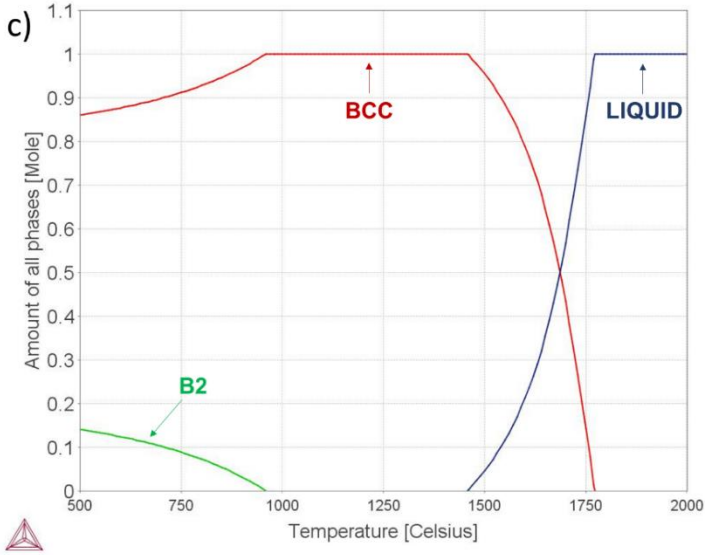
c)
BCC
LIQUID
B2
Amount of all phases [Mole]
Temperature [Celsius]

Figure 1: Evolution of phase fraction during solidification for (a) $(TiVNb)_{85}Cr_{15}$, (b) $(TiVNb)_{95.3}Co_{4.7}$ and (c) $(TiVNb)_{96.2}Ni_{3.8}$ alloys calculated by CALPHAD method (Thermo-Calc software® and TCHEA3 database).

Table 1: Calculated composition (%at.) of the equilibrium phases of the $(TiVNb)_{95.3}Co_{4.7}$ alloy at 1090 ºC and $(TiVNb)_{96.2}Ni_{3.8}$ at 900 ºC (Thermo-Calc software® and TCHEA3 database)

Alloy	Phase	Ti	V	Nb	Co	Ni
$(TiVNb)_{95.3}Co_{4.7}$	**BCC**	31.22	32.40	32.63	3.75	-
	B2	50.66	9.81	1.90	37.63	-
$(TiVNb)_{96.2}Ni_{3.8}$	**BCC**	31.67	32.55	32.81	-	2.95
	B2	44.0	17.1	9.2	-	29.6

XRD analysis of the as-cast alloys (Figure 2) confirmed that the three alloys are predominantly BCC. Low intensity peaks around $2\theta = 42$ º in the XRD pattern of the $(TiVNb)_{96.2}Ni_{3.8}$ alloy suggest the presence of small fraction of a secondary phase. The Rietveld refinements for the as-cast alloys are shown in Figure S1 of the supplementary data file. The BCC lattice parameters of $(TiVNb)_{85}Cr_{15}$, $(TiVNb)_{95.3}Co_{4.7}$ and $(TiVNb)_{96.2}Ni_{3.8}$ are listed in Table 2. Despite that Cr, Co and Ni have the same metal atom size (1.25 pm [21]), the lattice parameter for $(TiVNb)_{85}Cr_{15}$ alloy is smaller than the other two alloys as well as the equimolar composition TiVNb reported earlier [21]. This is explained by the larger Cr concentration (15 at%) as compared to 4.7 and 3.8 at% for Co and Ni, respectively.

Table 2: Valence electron concentration (VEC) and lattice parameters (a_{BCC}, a_{FCC}) for as-cast, hydrides and cycled samples after 1 and 20 cycles of hydrogenation.

Alloy	VEC	a_{BCC} (Å) As cast	a_{FCC} (Å) 1st cycle	a_{BCC} (Å) 1st cycle	a_{FCC} (Å) 20th cycle	a_{BCC} (Å) 20th cycle
TiVNb [21]	4.67	3.2000	4.4296	-	-	-
$(TiVNb)_{85}Cr_{15}$	4.87	3.164(1)	4.405(1)	3.167(1)	4.390(1)	3.167(1)
$(TiVNb)_{95.3}Co_{4.7}$	4.87	3.188(1)	4.411(1)	3.190(1)	4.431(1)	3.209(1)
$(TiVNb)_{96.2}Ni_{3.8}$	4.87	3.191(1)	4.424(1)	3.198(1)	4.417(1)	3.197(1)

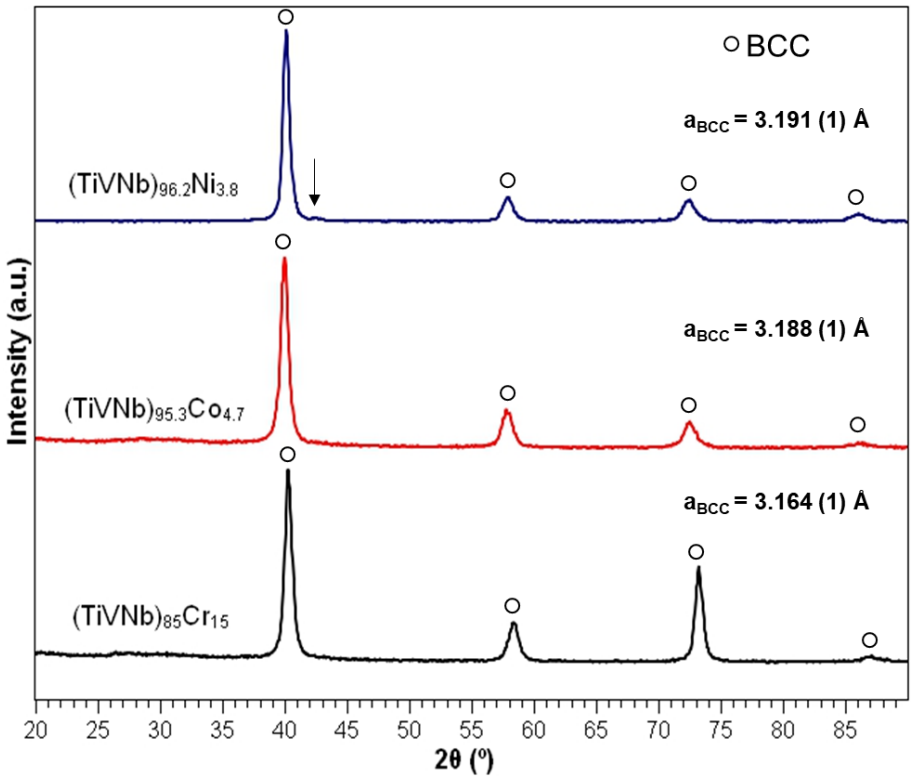

Figure 2: XRD patterns of as-cast samples confirming the formation of the predominantly BCC solid solution.

The as-cast samples presented dendritic microstructure as can be seen in the SEM-BSE images in Figures 3 (a)-(f). EDS analyses were carried out in the regions indicated by the numbered yellow marks. The overall chemical composition as well as the chemical composition in the middle of the dendrites and in interdendritic regions were measured for each sample. The results are displayed in Table 3 and show that the overall composition of the three alloys are reasonably close to the nominal ones. This was expected since there was no substantial mass loss of any element during arc melting procedure. The $(TiVNb)_{85}Cr_{15}$ alloy presented a better chemical homogeneity compared to the other two alloys. The composition of the interdendritic regions of the $(TiVNb)_{85}Cr_{15}$ was slightly richer in Ti and Cr and slightly poorer in Nb than the compositions measured in the middle of the dendrites. The higher chemical homogeneity of the $(TiVNb)_{85}Cr_{15}$ can be related to the smaller solidification interval predicted by thermodynamic calculations when compared to the other alloys.

The compositions measured at the middle of the dendritic region of the $(TiVNb)_{95.3}Co_{4.7}$ alloy is remarkably close to the composition of the BCC phase presented in Table 1. In addition, the composition measured in the interdendritic region is also close to the composition of the B2 phase predicted by the thermodynamic calculation (see Table 1), which confirms the

presence of this phase in the interdendritic region. The interdendritic region of the $(TiVNb)_{96.2}Ni_{3.8}$ alloy is Ti and Ni-rich, which also suggests the presence of a secondary phase. Although the thermodynamic calculation predicted that this alloy would crystallize as single BCC under equilibrium condition, it also predicted a large solidification interval (of approximately 300 ºC). Therefore, considerable solute partitioning is expected to occur during solidification out of equilibrium conditions, resulting in formation of secondary phases in the interdendritic regions. The chemical composition of the BCC phase and the B2 ordered phase, predicted to be in equilibrium at 900 ºC for the $(TiVNb)_{96.2}Ni_{3.8}$ alloy was presented in Table 1. The calculated composition of the B2 phase is also very close to the ones measured at the interdendritic regions for this alloy (Table 2), indicating the formation of some fraction of this intermetallic. EDS mapping for the three alloys are presented in Figure 4 (a), (b) and (c). By analyzing the Co-rich and Ni-rich regions in Figure 4 (b) and (c), respectively, one can see that the fraction of Co-rich intermetallic in the $(TiVNb)_{95.3}Co_{4.7}$ is lower when compared to the Ni-rich in the $(TiVNb)_{96.2}Ni_{3.8}$. The small intensity peaks presented in the XRD pattern of the $(TiVNb)_{96.2}Ni_{3.8}$ must be related to this intermetallic phase. It is worth noting that the small intensity of the diffraction peaks confirms the low fraction of this phase.

The important aspect to be highlighted is that the compositions of the major BCC phases measured in the middle of the dendritic regions were relatively close to the target ones for the three alloys. More importantly, VEC values calculated using these compositions varies from 4.78 to 4.87, which is a small range. Therefore, we succeed to produce three different BCC alloys with similar VEC values.

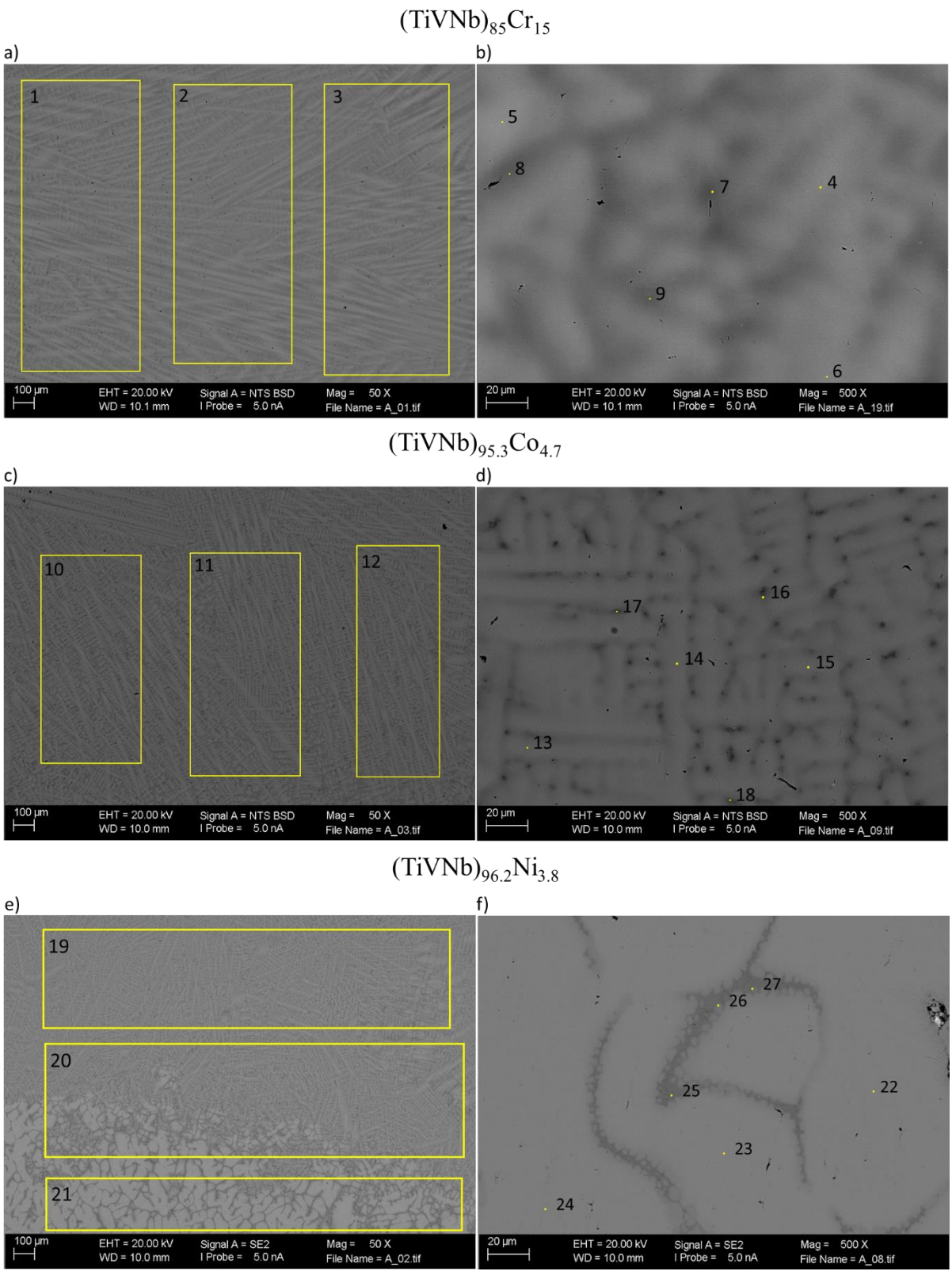

Figure 3: BSE images of samples in as cast condition showing dendritic structure in low and higher magnification (a),(b) $(TiVNb)_{85}Cr_{15}$ (c),(d) $(TiVNb)_{95.3}Co_{4.7}$ (e),(f) $(TiVNb)_{96.2}Ni_{3.8}$ – black numbers and yellow marks indicate regions where chemical composition analysis via EDS were performed.

Table 3: Chemical composition in at.% of as cast alloys obtained from the overall, dendritic and interdendritic regions indicated in Figure 3 by black numbers and yellow marks.

Alloy	Region	Spectrum	Ti	V	Nb	Cr	Co	Ni	VEC
$(TiVNb)_{85}Cr_{15}$	Overall	1	28.7	28.4	28.2	14.7	-	-	4.86
		2	28.6	28.4	28.3	14.7	-	-	4.86
		3	28.6	28.5	28.3	14.7	-	-	4.87
	Dendritic	4	26.4	27.5	33.4	12.8	-	-	4.87
		5	25.9	27.0	35.8	11.3	-	-	4.85
		6	27.0	27.8	32.4	12.7	-	-	4.85
	Interdendritic	7	32.9	28.1	20.8	18.2	-	-	4.85
		8	31.5	28.5	23.1	16.8	-	-	4.85
		9	31.7	28.5	22.8	17.0	-	-	4.85
$(TiVNb)_{95.3}Co_{4.7}$	Overall	10	32.1	31.7	31.7	-	4.5	-	4.86
		11	32.2	31.8	31.4	-	4.5	-	4.85
		12	32.7	31.6	31.2	-	4.6	-	4.86
	Dendritic	13	29.8	31.3	35.4	-	3.5	-	4.84
		14	30.7	31.8	33.9	-	3.5	-	4.83
		15	29.5	31.4	35.4	-	3.7	-	4.85
	Interdendritic	16	49.5	9.7	5.5	-	35.3	-	5.92
		17	45.9	17.7	11.2	-	25.2	-	5.55
		18	46.4	10.6	6.8	-	36.2	-	5.98
$(TiVNb)_{96.2}Ni_{3.8}$	Overall	19	33.1	32.0	30.3	-	-	4.5	4.89
		20	33.1	31.8	30.5	-	-	4.5	4.90
		21	31.9	31.6	33.3	-	-	3.3	4.84
	Dendritic	22	31.6	32.6	33.7	-	-	2.1	4.79
		23	31.7	32.3	33.7	-	-	2.3	4.80
		24	32.0	32.3	33.6	-	-	2.1	4.78
	Interdendritic	25	48.1	12.1	7.1	-	-	32.7	6.15
		26	47.7	12.4	7.4	-	-	32.4	6.14
		27	51.5	10.9	6.5	-	-	31.2	6.04

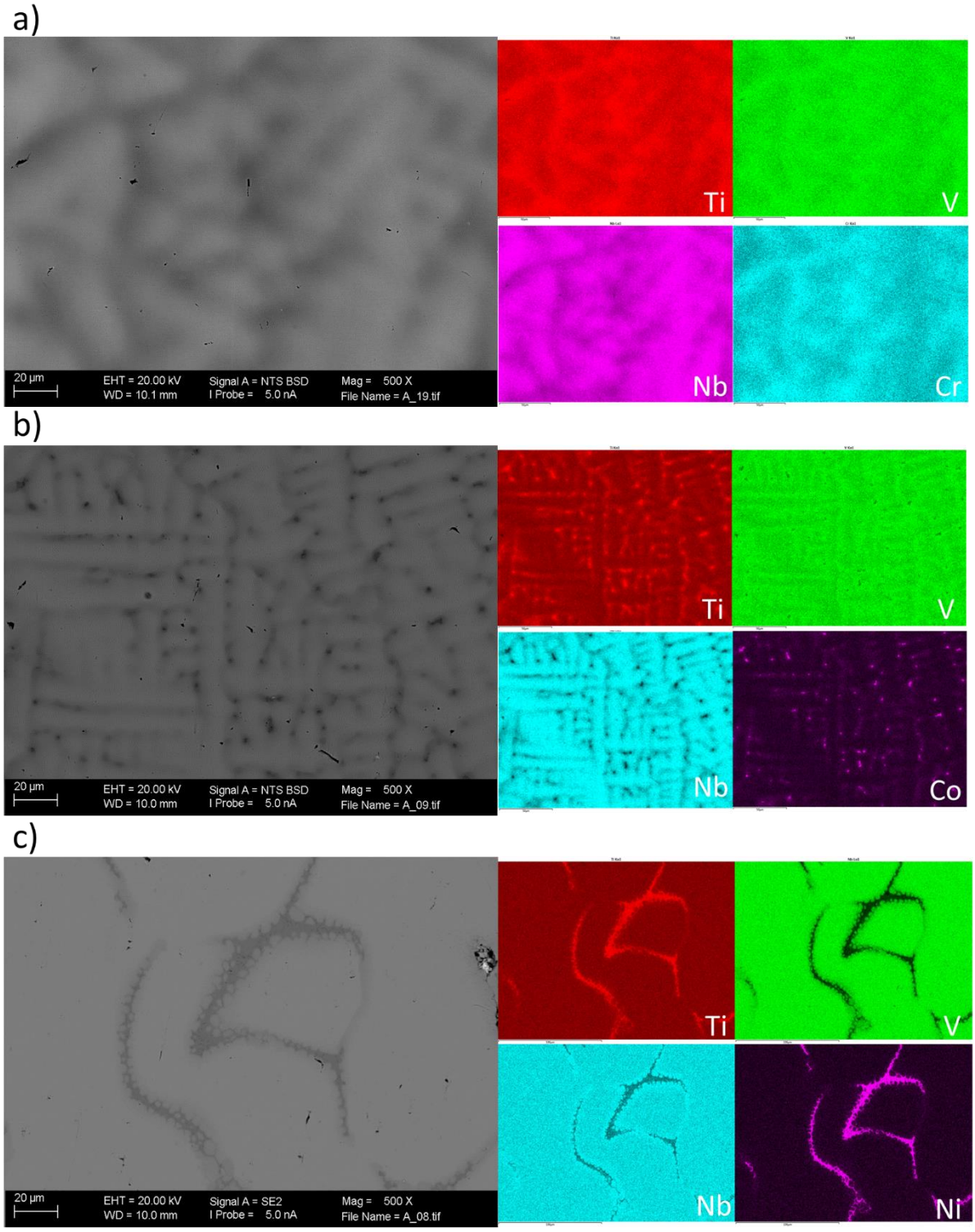

Figure 4: EDS mapping analysis of as cast alloys a) $(TiVNb)_{85}Cr_{15}$ b) $(TiVNb)_{95.3}Co_{4.7}$ c) $(TiVNb)_{96.2}Ni_{3.8}$.

3.2 Hydrogen storage properties

Figure 5 (a) presents the hydrogen absorption kinetics at room temperature for the three alloys. A short incubation time of 0.1-1.6 minutes is observed prior to any considerable hydrogen absorption. Subsequently, a large amount of hydrogen is absorbed (~2 H/*M*) with fast kinetic in less than 1 minute for all the alloys. The hydrogenation process in these alloys leads to the formation of FCC dihydrides, as identified by XRD patterns displayed in Figure 5 (b). The formation of FCC dihydrides is in agreement with results reported earlier for other BCC alloys [28–30] and high entropy alloys [17,21,22]. The maximum hydrogen gravimetric capacities vary between 3.11 and 3.18 wt.% and they are superior than the values reported for some intermetallic alloys such as, TiFe (1.89 wt.%) [31], $LaNi_5$ (1.4 wt.%) [31], and some BCC alloys as TiV_2 (2.6 wt.%) [31], $V_{40}Ti_{21.5}Cr_{38.5}$ (2.44 wt.%) [32], $V_{20}Ti_{32}Cr_{48}$ (2.90 wt.%) [32]. These values are in good agreement with the 3 wt.% reported for the equimolar TiVNb also forming a dihydride phase [21]. The lattice parameter of the FCC hydrides are listed in Table 2. The lattice parameters of the FCC dihydride $(TiVNb)_{85}Cr_{15}H_x$ presented a smaller value than the dihydrides of the other two alloys and the dihydride of the equimolar TiVNb composition [21]. The corresponding Rietveld refinements are presented in Figure S2 of the supplementary data file.

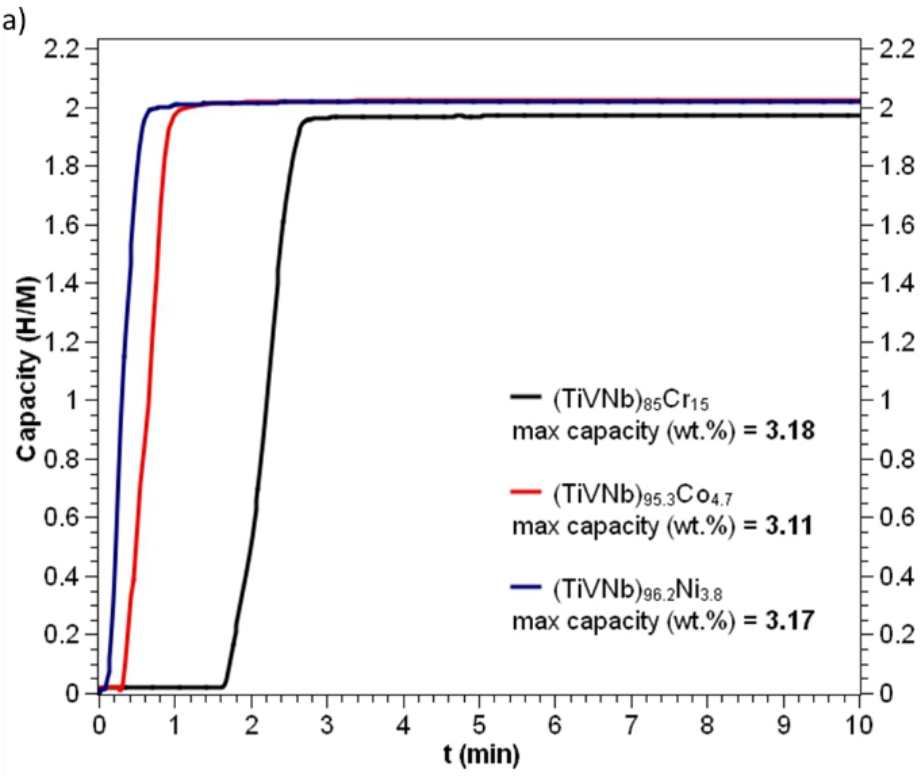

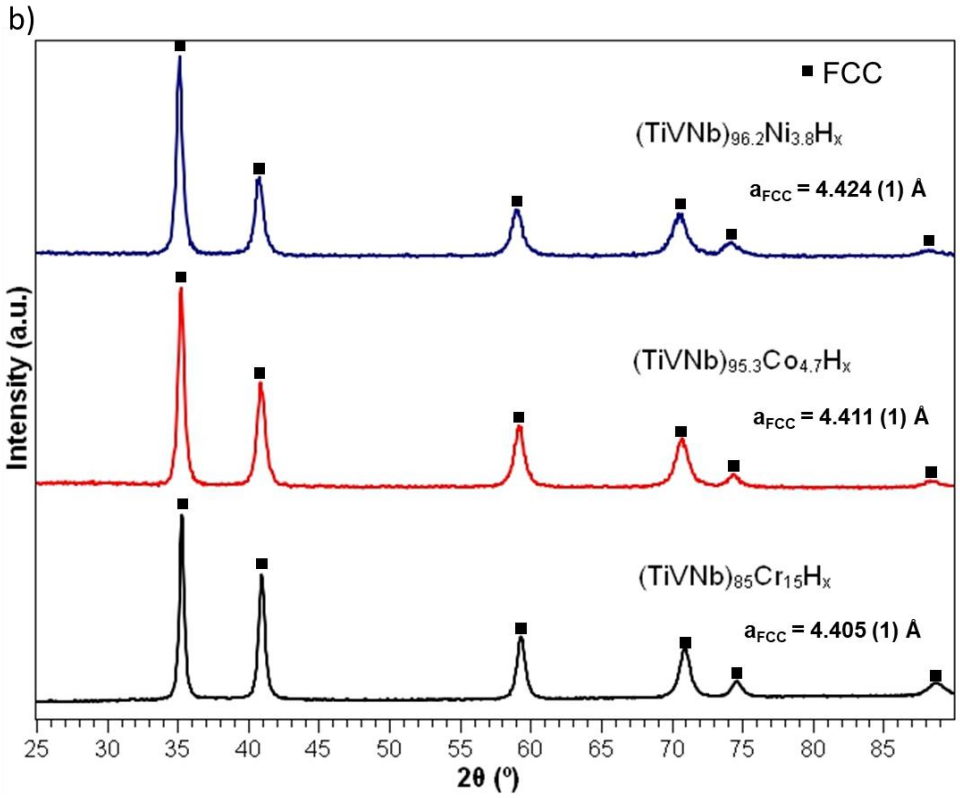

Figure 5: (a) Measurements of hydrogen absorption kinetics at room temperature (b) XRD patterns after kinetic measurements showing dihydride formation with single-phase FCC structure for the $(TiVNb)_{85}Cr_{15}$, $(TiVNb)_{95.3}Co_{4.7}$ and $(TiVNb)_{96.2}Ni_{3.8}$ alloys.

Figure 6 (a), (b) and (c) show the PCI measurements for the three alloys, which demonstrate a similar two step sequence of hydrogenation. The alloys initially absorb around 0.7-0.9 H/M in a first plateau at low equilibrium pressures and subsequently absorb hydrogen during a second plateau at higher equilibrium pressures reaching final capacities of 1.6-2.0 H/M. Although it has been reported that absorption for different multicomponent BCC alloys takes place in a single plateau, indicating a single phase transition from BCC solid solution to FCC/ BCT hydride [11,12,17,20], there are also examples of alloys, such as TiZrNbHfTa [19], TiVNbCr, TiVNbMo [21] that shows the formation of an intermediate monohydride prior to the formation of the FCC-dihydride. In this work, the PCI diagrams have two well defined plateaus suggesting the formation of an intermediate monohydride before the formation of the FCC-dihydride. Sakaki et al. [28] also observed a two-step reaction of hydrogenation for BCC Nb-based alloys ($Nb_{40}Ti_{42}Cr_{18}$, $Nb_{50}Ti_{35}Cr_{15}$ and $Nb_{60}Ti_{28}Cr_{12}$) and they reported the sequence (BCC → BCC monohydride→ FCC dihydride). Therefore, we performed a PCI measurement

up to 0.83 H/M for $(TiVNb)_{85}Cr_{15}$ alloy to check the intermediate structure of the monohydride, which was identified as a BCC phase with larger lattice parameter (a_{BCC} = 3.282(1)) than the as cast sample (a_{BCC} = 3.164(1)). The Rietveld refinement of this sample is presented in Figure S3 of the supplementary file. Another aspect to be noticed is the presence of hysteresis in all PCIs at high temperatures. The desorption curves presented equilibrium pressures at least with one order of magnitude lower than the absorption curves. It is also important to highlight that all the alloys displayed similar behavior in the equilibrium pressures values of the second plateau as function of temperature. This becomes clear observing the Van't Hoff plots of each alloy in Figure 6 (d): the plots are parallel and almost overlap, especially for the absorption reaction. This is consistent with the similar values of the plateau enthalpy and entropy determined by Van't Hoff equation (Table 4). For the absorption reaction, the enthalpy values varied between -64 and -67 kJ/mol H_2 and the entropy values between -164 and -174 J/K·mol H_2. For the desorption curves these values were between -64 and -70 kJ/mol H_2 for the enthalpy and -143 and -156 J/K·mol H_2 for the entropy. The enthalpy values are comparable to Mg_2Ni hydride (-65 kJ/mol H_2 [33]) and TiVZrNbHf hydride (-59 kJ/mol H_2 [12]), but larger than hydrides of $LaNi_5$ related intermetallic compounds (-30 -35 kJ/mol H_2 [33]).

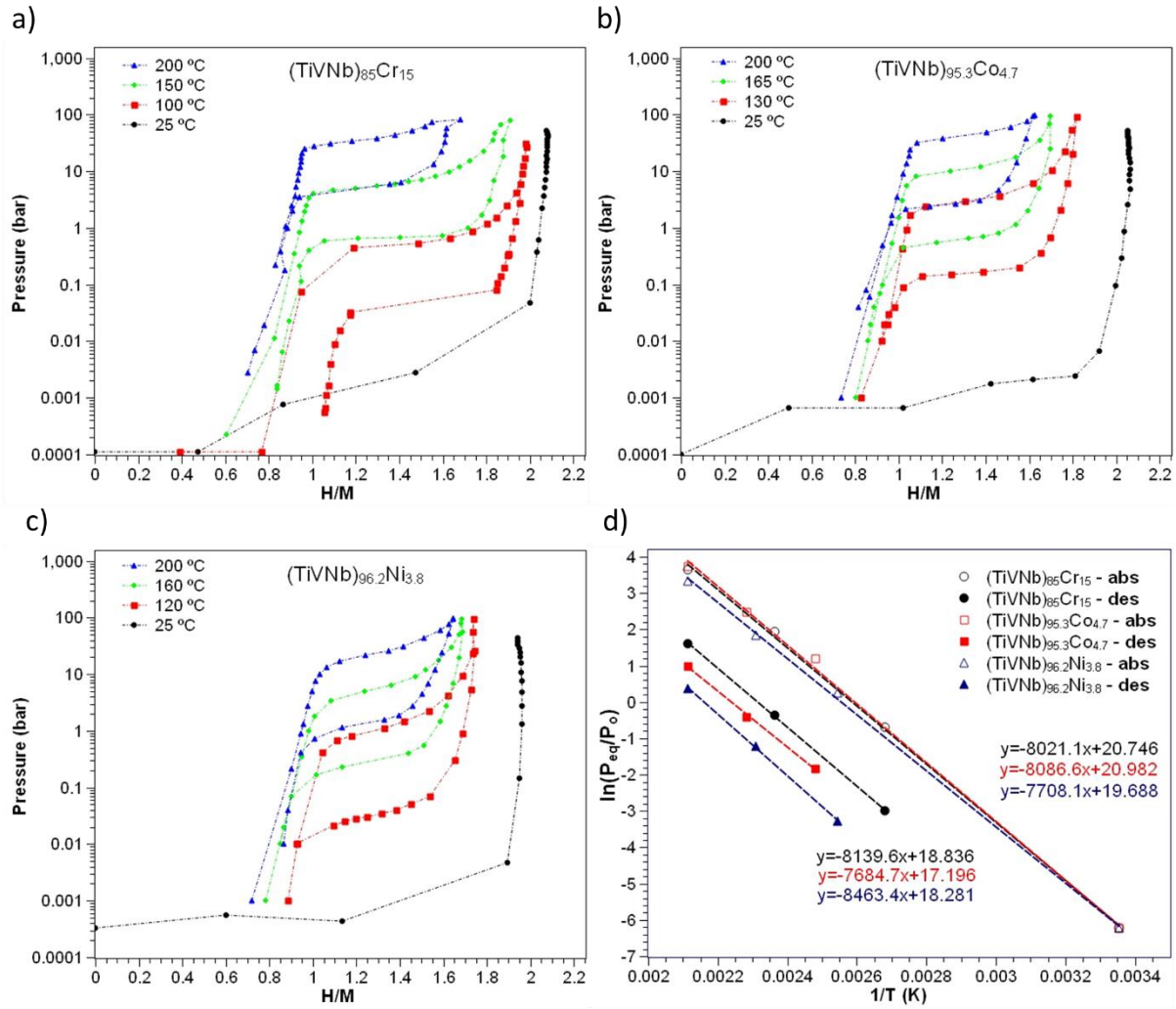

Figure 6: Pressure-Composition-Isotherms of a) $(TiVNb)_{85}Cr_{15}$, b) $(TiVNb)_{95.3}Co_{4.7}$ and c) $(TiVNb)_{96.2}Ni_{3.8}$ alloys and d) Van't Hoff plots.

Table 4: Plateau enthalpy and entropy of $(TiVNb)_{85}Cr_{15}$, $(TiVNb)_{95.3}Co_{4.7}$ and $(TiVNb)_{96.2}Ni_{3.8}$ alloys determined by Van't Hoff analyses in absorption and desorption measurements.

Alloy	ΔH_{abs} (kJ/mol H_2)	ΔH_{des} (kJ/mol H2)	ΔS_{abs} (J/K mol H2)	ΔS_{des} (J/K mol H2)
$(TiVNb)_{85}Cr_{15}$	- 67 ± 2	- 68 ± 1	- 172 ± 4	- 156 ± 3
$(TiVNb)_{95.3}Co_{4.7}$	- 67 ± 2	- 64 ± 3	- 174 ± 5	- 143 ± 7
$(TiVNb)_{96.2}Ni_{3.8}$	- 64 ± 1	- 70 ± 2	- 164 ± 3	- 152 ± 4

Measurements of hydrogen absorption/desorption cycling are shown in Figure 7 for all alloys. The small reduction in capacity noticed at the first cycles for all alloys might be justified by the increase of crystalline defects as dislocations and grain boundaries which is known to diminish the hydrogen storage content in a metallic phase [34]. The $(TiVNb)_{85}Cr_{15}$ alloy shows a continuous reduction in capacity from 3.18 wt.% to 2.88 wt.% after 20 cycles, which corresponds to 1.79 H/M. The continuous fading of capacity over cycling is also reported for other ternary BCC alloys (TiVCr and TiNbCr) and it is often associated to phase segregation resulting in a secondary phase formation [30,32,35]. On the other hand, despite a pronounced reduction of capacity during the first two cycles, $(TiVNb)_{95.3}Co_{4.7}$ and $(TiVNb)_{96.2}Ni_{3.8}$ alloys show a more stable behavior reaching capacities of 2.77 wt.% after 20 cycles, which correspond to 1.76 H/M. In terms of cyclability, the performance of these alloys surpass those reported for many binary and ternary BCC alloys [29,30,32,35–39] and new multicomponent, high entropy and complex concentrated alloys [17,20,21].

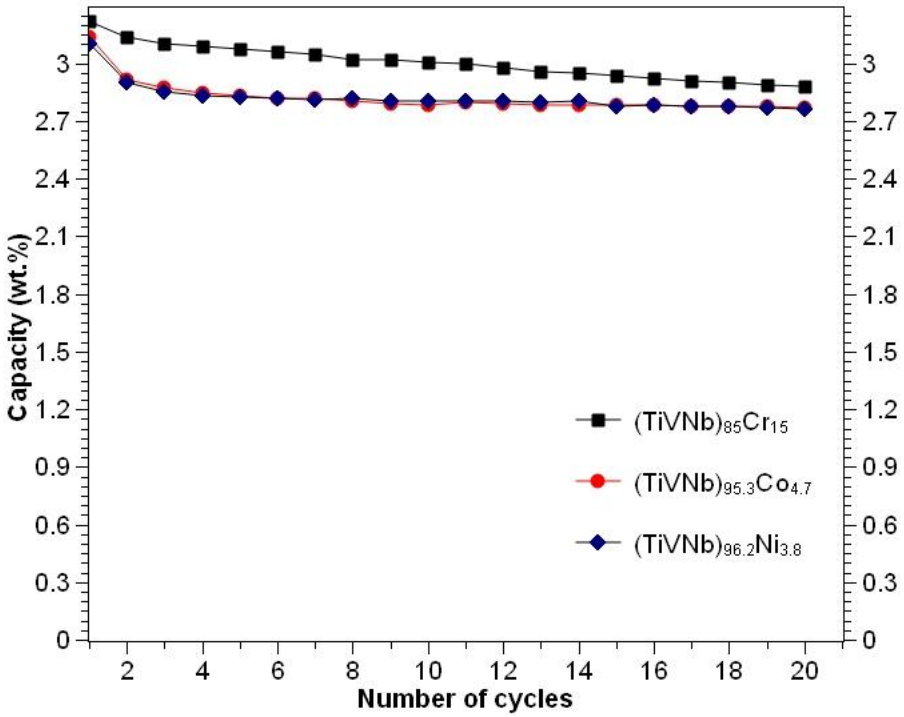

Figure 7: Hydrogen absorption capacity in wt.% of $(TiVNb)_{85}Cr_{15}$, $(TiVNb)_{95.3}Co_{4.7}$ and $(TiVNb)_{96.2}Ni_{3.8}$ alloys over the number of cycles of absorption and desorption.

To better understand the storage capacity loss over cycling, each alloy was characterized by XRD in the absorbed and desorbed conditions after the first and the twentieth cycle. Figures 8 (a), (b) and (c) display the XRD patterns after the first and 20th cycle for $(TiVNb)_{85}Cr_{15}$, $(TiVNb)_{95.3}Co_{4.7}$ and $(TiVNb)_{96.2}Ni_{3.8}$, respectively. The values of the lattice

parameters for hydrides and desorbed phases are listed in Table 2. The related Rietveld refinements can be found in Figure S4 of the supplementary data file. For the three alloys, small changes in lattice parameters were observed for the FCC hydrides after cycling. The same was observed comparing the lattice parameters of the desorbed conditions from the first and twentieth cycle. The FCC hydrides $(TiVNb)_{85}Cr_{15}H_x$ and $(TiVNb)_{96.2}Ni_{3.8}H_x$ presented a slight reduction in lattice parameters values after cycling, which agrees with the reduction in capacity observed over cycling. On the other hand, the FCC hydride $(TiVNb)_{95.3}Co_{4.7}H_x$ presented an increase of lattice parameter after cycling despite the reduction in capacity, which is contradictory to the loss in capacity observed for this alloy. However, it should be noticed that a small peak of a secondary phase (indicated by the black arrow in Figure 8 (b)) was detected in the XRD pattern of the desorbed condition after 20 cycles. This peak was not detected in the as cast sample or in the desorbed sample after the first cycle, indicating that is a result of the cycling procedure. Based on Thermo-calc calculations, the segregation observed is probably rich in Co. This Co segregation might explain the increase in lattice parameters observed in both samples (hydride phase and desorbed) after 20 cycles, since the predominant phase would be richer in Ti, V and Nb which present larger atomic sizes. Moreover, it is important to highlight the broadening of the peaks in the patterns after 20 cycles. This phenomenon was already reported in the literature and it is related to crystallite size refinement, increase of defects and the increase of lattice strain during repeated hydrogenation processes [17,20,36,40]. Another important remark in Figure 8 (a) is a small peak (marked with star) of a BCC phase with lattice parameter of a_{BCC} = 3.281 Å in the absorbed sample of the $(TiVNb)_{85}Cr_{15}$ alloy after 20 cycles. This peak is not observed in the desorbed sample after 20 cycles. We suggest that this phase correspond to the BCC monohydride since the lattice parameter found is the same of the sample hydrogenated up to 0.83 H/*M*. This indicates incomplete transformation from BCC monohydride to FCC dihydride, which suggests that the reduction of the reversible capacity is related to incomplete absorption rather than incomplete desorption during hydrogenation cycling. We suggest that the differences in capacity loss behavior between $(TiVNb)_{85}Cr_{15}$ and the other two alloys are linked to this incomplete absorption.

a)

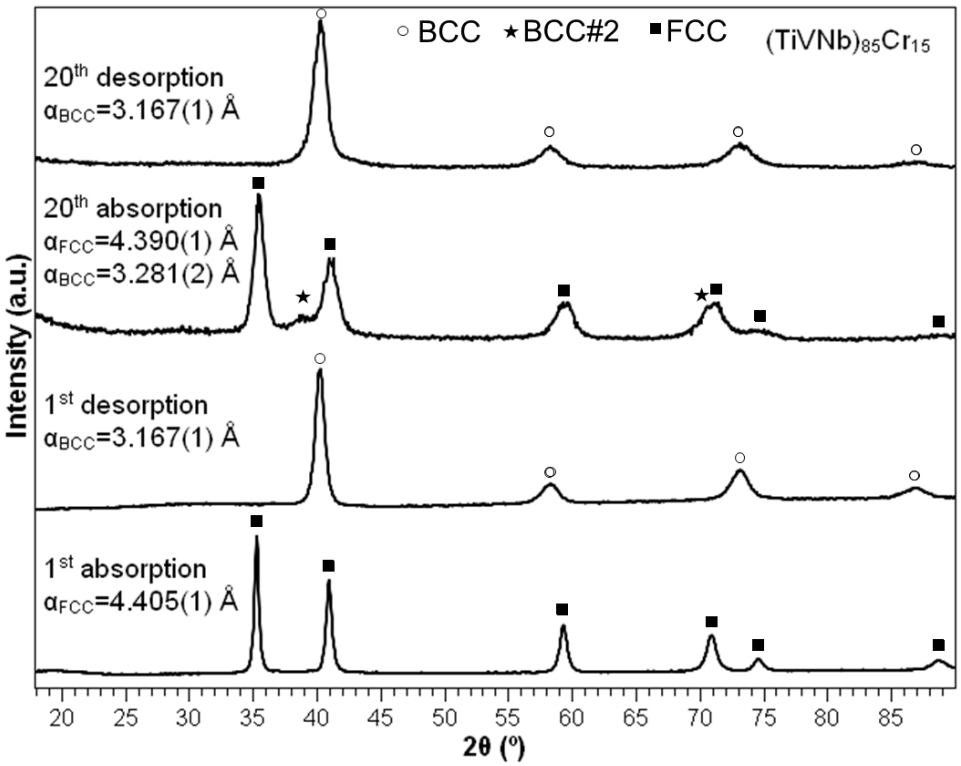
○ BCC ★BCC#2 ■FCC
(TiVNb)85Cr15
20th desorption
αBCC=3.167(1) Å
20th absorption
αFCC=4.390(1) Å
αBCC=3.281(2) Å
1st desorption
αBCC=3.167(1) Å
1st absorption
αFCC=4.405(1) Å
Intensity (a.u.)
20 25 30 35 40 45 50 55 60 65 70 75 80 85
2θ (º)

b)

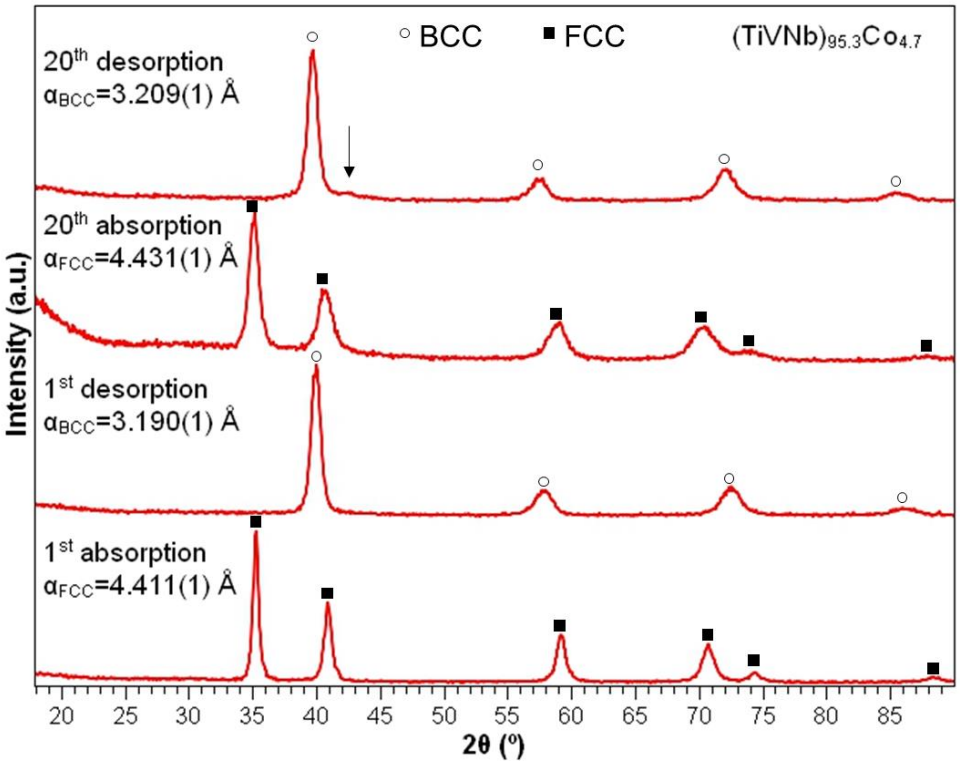
○ BCC ■ FCC
(TiVNb)95.3Co4.7
20th desorption
αBCC=3.209(1) Å
20th absorption
αFCC=4.431(1) Å
1st desorption
αBCC=3.190(1) Å
1st absorption
αFCC=4.411(1) Å
Intensity (a.u.)
20 25 30 35 40 45 50 55 60 65 70 75 80 85
2θ (º)

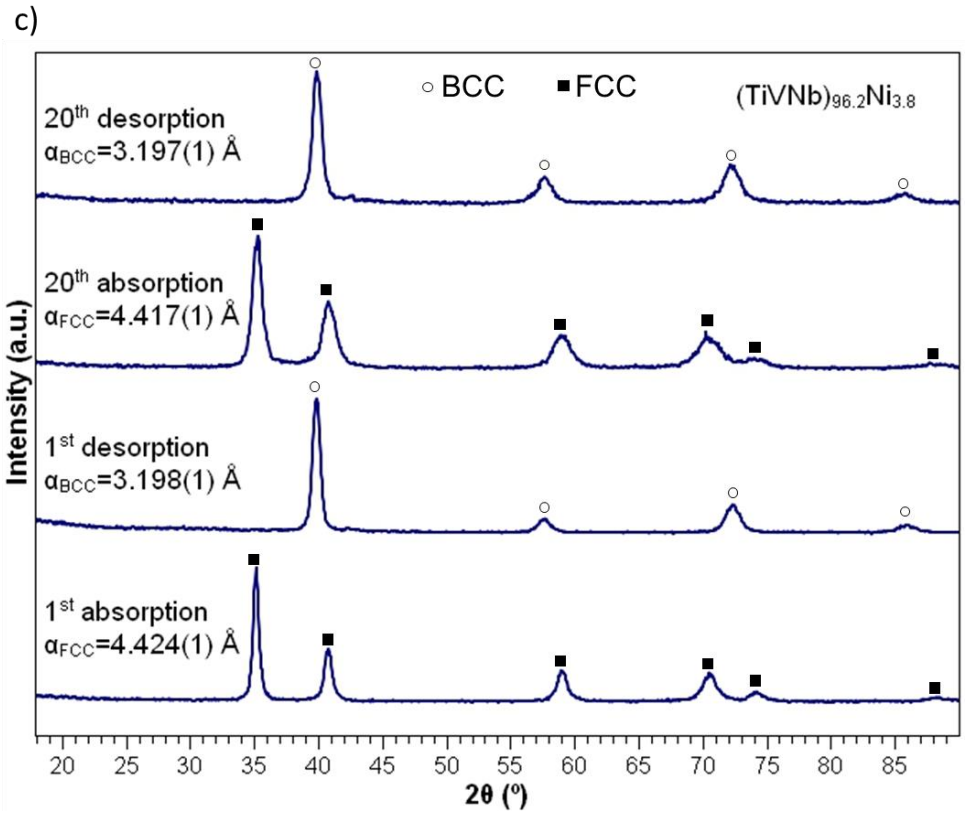

Figure 8: XRD patterns of as absorbed and desorbed samples from the first and twentieth cycles of each alloy a) $(TiVNb)_{85}Cr_{15}$ b) $(TiVNb)_{95.3}Co_{4.7}$ c) $(TiVNb)_{96.2}Ni_{3.8}$.

Further understanding of the cycling effect was brought by TDS measurements. Figures 9 (a), (b) and (c) show the thermo-desorption behavior in the first and twentieth cycle of $(TiVNb)_{85}Cr_{15}H_x$, $(TiVNb)_{95.3}Co_{4.7}H_x$ and $(TiVNb)_{96.2}Ni_{3.8}H_x$ hydrides, respectively. The desorption curves from the first cycle of each sample show multiple step desorption events in large temperature ranges. For $(TiVNb)_{85}Cr_{15}$ this range was 50-400 ºC, whereas for $(TiVNb)_{95.3}Co_{4.7}$ was 85-390 ºC and for $(TiVNb)_{96.2}Ni_{3.8}$ was 135-420 ºC The onset temperatures for hydrogen desorption of each hydride are listed in Table 5.

Table 5: Valence electron concentration (VEC) and onset temperatures (T_{onset}) of hydrogen desorption for hydrides after 1 and 20 cycles of hydrogenation.

Alloy	**VEC**	**T_{onset} (ºC) 1st cycle**	**T_{onset} 20th cycle**
TiVNb [21]	4.67	280	-
$(TiVNb)_{85}Cr_{15}$	4.87	51	163
$(TiVNb)_{95.3}Co_{4.7}$	4.87	89	210

$(TiVNb)_{96.2}Ni_{3.8}$	4.87	136	210

The hydride $(TiVNb)_{85}Cr_{15}H_x$ presents the lowest onset temperature among the three hydrides, followed by $(TiVNb)_{95.3}Co_{4.7}H_x$ and $(TiVNb)_{96.2}Ni_{3.8}H_x$. Additionally, the three hydrides showed lower onset temperatures than the equimolar composition of TiVNb [21]. This indicates that the desorption behavior was affected by the Cr, Co and Ni substitution and not only by the VEC. Regarding the measurements after cycling, the three alloys presented similar changes in the TDS profile: a desorption profile with two distinct peaks and a shift of the onset temperature towards higher values. The onset temperatures of each hydride after 20 cycles are also listed in Table 5. Similar to the trend observed for the samples of the first cycle, $(TiVNb)_{85}Cr_{15}H_x$ showed the lowest onset temperature among the three hydrides. However, $(TiVNb)_{95.3}Co_{4.7}H_x$ had the same onset temperature that $(TiVNb)_{96.2}Ni_{3.8}H_x$ deviating from this same trend. This deviation might be explained by the Co segregation detected in the sample after cycling. Nevertheless, the range of desorption temperatures of each hydride changed after cycling. For $(TiVNb)_{85}Cr_{15}H_x$ this range was 150-450 ºC, for $(TiVNb)_{95.3}Co_{4.7}H_x$ the range was 200-450 ºC and for $(TiVNb)_{96.2}Ni_{3.8}H_x$ the range was 150-450 ºC. It is important to state that the increase of onset temperatures and the variations in the range of desorption temperatures could be associated to the microstructural changes (increase of crystal defects) during cycling.

Regarding the two step desorption event that become very clear after cycling, Nygard et al. [21] also reported similar thermo desorption profiles for a series of high entropy alloys, including the equimolar TiVNb/TiVNbCr alloys and claimed that the first desorption event corresponds to the decomposition of the FCC dihydride into a BCC monohydride and the second event corresponds to the decomposition of the BCC monohydride into the hydrogen free alloy. Based on the two-step hydrogenation process observed in the PCI measurements and in the intermediate monohydride phase detected by XRD we consider this hypothesis valid for the desorption events observed in our study.

a)

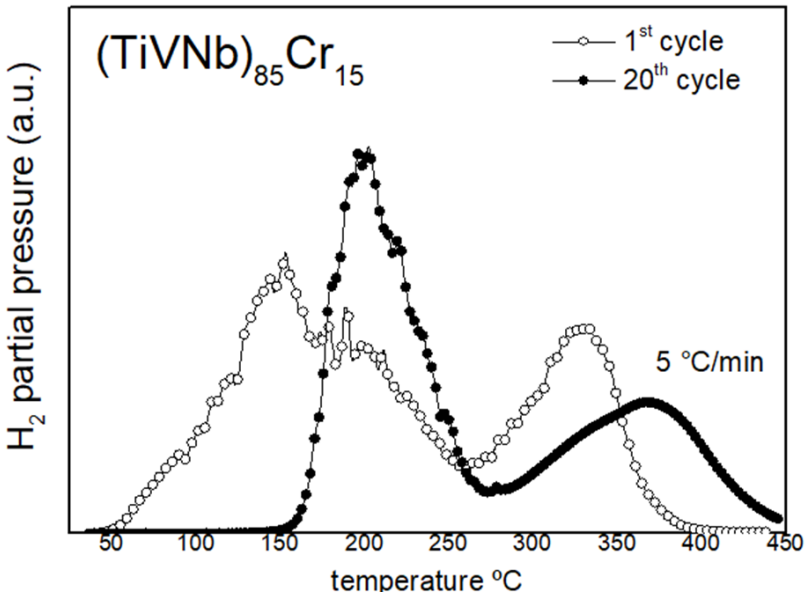
(TiVNb)85Cr15
1st cycle
20th cycle
5 °C/min
H2 partial pressure (a.u.)
50
100
150
200
250
300
350
400
450
temperature °C

b)

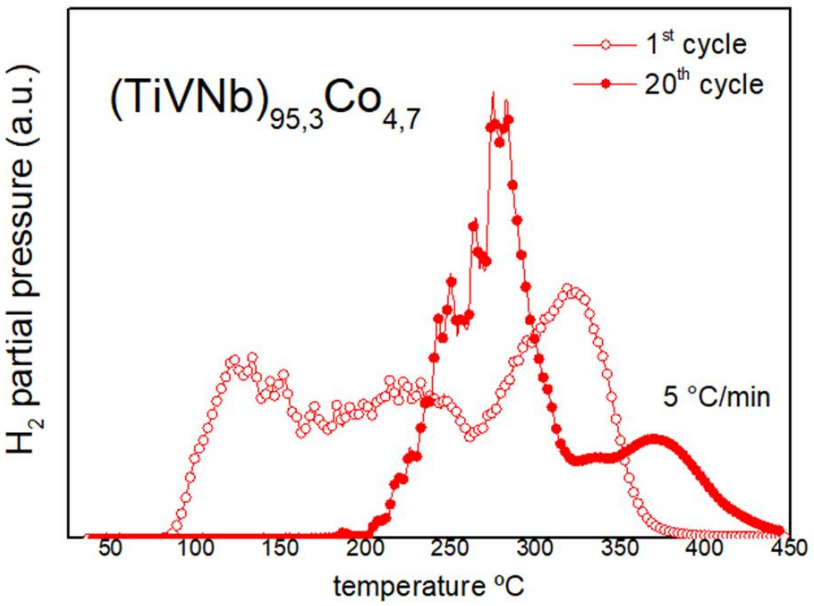
(TiVNb)95,3Co4,7
1st cycle
20th cycle
5 °C/min
H2 partial pressure (a.u.)
50
100
150
200
250
300
350
400
450
temperature °C

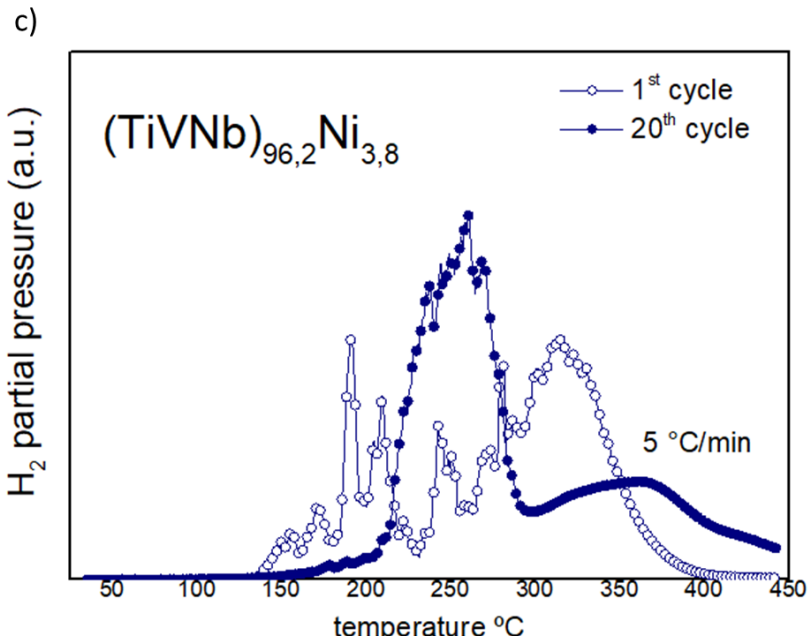

Figure 9: Thermo desorption profiles of hydrides samples from the first and twentieth cycle of hydrogenation a) $(TiVNb)_{85}Cr_{15}$ b) $(TiVNb)_{95.3}Co_{4.7}$ c) $(TiVNb)_{96.2}Ni_{3.8}$.

In agreement with the correlation of VEC parameter with hydrogen storage properties proposed by Nygard et al.[21], the three alloys studied in this work having the same VEC = 4.87 showed similar behavior in terms of maximum storage capacity and kinetics of absorption. Additionally, it was evidenced in this work that thermodynamic properties for hydride formation seems also to have a correlation with VEC parameter, since the three hydrides presented similar values of enthalpy and entropy formation energy despite the differences in chemical composition. This hypothesis needs to be further investigated for different systems of multicomponent alloys and with larger chemical compositional differences, but this might contribute for the development of new designing strategies of multicomponent alloys for hydrogen storage based on a thermodynamic point of view. On the other hand, the initial premise of spontaneous desorption for alloys with VEC > 4.75, as proposed recently in the literature, was not observed in our study. In fact, the PCIs at RT of the three alloys showed equilibrium pressures in absorption for the second plateau lower than 0.01 bar, which considering the hysteresis effect, would be at least one order of magnitude lower in desorption conditions. Moreover, the differences in desorption behavior observed in this study and the effects of cycling on storage capacity suggest that other parameters should also be taken into account for a complete and efficient description of hydrogen storage properties in

multicomponent alloys. Microstructural changes, chemical segregation, induced strain due to hydrogenation process are some of the sources that seems also to affect the desorption and cycling properties of a hydride from a multicomponent alloy.

4. Conclusions

Three multicomponent alloys predominantly with a BCC structure and with the same VEC values were successfully designed and produced, namely $(TiVNb)_{85}Cr_{15}$, $(TiVNb)_{95.3}Co_{4.7}$ and $(TiVNb)_{96.2}Ni_{3.8}$. Under hydrogen pressure, the alloys formed FCC hydrides at room temperature, reaching a maximum hydrogen uptake of 2 H/M (3.1-3.2 wt.%) in a few minutes demonstrating fast absorption kinetics. PCI measurements showed similar two step sequence of hydrogenation that was related to the formation of an intermediate BCC monohydride resulting in the following sequence of hydrogenation: BCC alloy → BCC monohydride → FCC dihydride. Thermodynamic properties of hydride formation were obtained for the three alloys and presented similar values despite the differences in chemical composition. Excellent hydrogen storage capacities around 2.77-2.88 wt.% were found for the three alloys after 20 cycles of absorption and desorption. Although $(TiVNb)_{85}Cr_{15}$ presented a continuous fading in capacity, $(TiVNb)_{95.3}Co_{4.7}$ and $(TiVNb)_{96.2}Ni_{3.8}$ showed a more stable behavior after a small loss in capacity during the first cycles. This difference was associated to incomplete transformation of BCC monohydride to FCC dihydride in the $(TiVNb)_{85}Cr_{15}$ alloy after cycling which was not detected in $(TiVNb)_{95.3}Co_{4.7}$ or $(TiVNb)_{96.2}Ni_{3.8}$ alloys. Thermo desorption analyses indicated a two-step event in agreement with PCI measurements, but the desorption behavior varied among the alloys and for different cycling conditions. Nevertheless, we acknowledge the effect of VEC parameter in hydrogen storage properties, especially in the maximum storage capacity and possibly in the thermodynamic properties for hydride formation, but desorption properties and reversibility characteristics demonstrated to be affected to other factors as well, for example microstructural changes.

Acknowledgments

This work was financed in part by the Serrapilheira Institute (grant number Serra-1709-17362), in part by the Conselho Nacional de Desenvolvimento Científico e Tecnológico - CNPq (Project number: 142446/2019-0) and in part by the CAPES-COFECUB cooperation program process number 88887.387430/2019-00, project number 88887.191910/2018-00. This study was financed in part by the Coordenação de Aperfeiçoamento de Pessoal de Nível

Superior - Brasil (CAPES) - Finance Code 001, Federal University of Sao Carlos, Graduate Program in Materials Science and Engineering.

Data statement

The data used in this manuscript is available for reproduction upon request.

5. References

[1] A. Züttel, A. Remhof, A. Borgschulte, O. Friedrichs, Hydrogen: The future energy carrier, Philos. Trans. R. Soc. A Math. Phys. Eng. Sci. 368 (2010) 3329–3342. doi:10.1098/rsta.2010.0113.

[2] K.T. Møller, T.R. Jensen, E. Akiba, H. wen Li, Hydrogen - A sustainable energy carrier, Prog. Nat. Sci. Mater. Int. 27 (2017) 34–40. doi:10.1016/j.pnsc.2016.12.014.

[3] N.A.A. Rusman, M. Dahari, A review on the current progress of metal hydrides material for solid-state hydrogen storage applications, Int. J. Hydrogen Energy. 41 (2016) 12108–12126. doi:10.1016/j.ijhydene.2016.05.244.

[4] M. Dornheim, Thermodynamics of Metal Hydrides: Tailoring Reaction Enthalpies of Hydrogen Storage Materials, Thermodyn. - Interact. Stud. - Solids, Liq. Gases. (2011). doi:10.5772/21662.

[5] Q. Lai, Y. Sun, T. Wang, P. Modi, C. Cazorla, U.B. Demirci, J.R. Ares Fernandez, F. Leardini, K.F. Aguey-Zinsou, How to Design Hydrogen Storage Materials? Fundamentals, Synthesis, and Storage Tanks, Adv. Sustain. Syst. 3 (2019) 1–64. doi:10.1002/adsu.201900043.

[6] R. Moradi, K.M. Groth, Hydrogen storage and delivery: Review of the state of the art technologies and risk and reliability analysis, Int. J. Hydrogen Energy. 44 (2019) 12254–12269. doi:10.1016/j.ijhydene.2019.03.041.

[7] A. Züttel, Materials for hydrogen storage, Mater. Today. 6 (2003) 24–33. doi:10.1016/S1369-7021(03)00922-2.

[8] B. Sakintuna, F. Lamari-Darkrim, M. Hirscher, Metal hydride materials for solid hydrogen storage: A review, Int. J. Hydrogen Energy. 32 (2007) 1121–1140. doi:10.1016/j.ijhydene.2006.11.022.

[9] U. Eberle, M. Felderhoff, F. Schüth, Chemical and physical solutions for hydrogen storage, Angew. Chemie - Int. Ed. 48 (2009) 6608–6630. doi:10.1002/anie.200806293.

[10] D.B. Miracle, O.N. Senkov, A critical review of high entropy alloys and related concepts, Acta Mater. 122 (2017) 448–511. doi:10.1016/j.actamat.2016.08.081.

[11] M. Sahlberg, D. Karlsson, C. Zlotea, U. Jansson, Superior hydrogen storage in high entropy alloys, Sci. Rep. 6 (2016) 1–6. doi:10.1038/srep36770.

[12] D. Karlsson, G. Ek, J. Cedervall, C. Zlotea, K.T. Møller, T.C. Hansen, J. Bednarčík, M. Paskevicius, M.H. Sørby, T.R. Jensen, U. Jansson, M. Sahlberg, Structure and Hydrogenation Properties of a HfNbTiVZr High-Entropy Alloy, Inorg. Chem. 57

(2018) 2103–2110. doi:10.1021/acs.inorgchem.7b03004.

[13] H. Shen, J. Hu, P. Li, G. Huang, J. Zhang, J. Zhang, Y. Mao, H. Xiao, X. Zhou, X. Zu, X. Long, S. Peng, Compositional dependence of hydrogenation performance of Ti-Zr-Hf-Mo-Nb high-entropy alloys for hydrogen/tritium storage, J. Mater. Sci. Technol. (2020). doi:10.1016/j.jmst.2019.08.060.

[14] Y.F. Kao, S.K. Chen, J.H. Sheu, J.T. Lin, W.E. Lin, J.W. Yeh, S.J. Lin, T.H. Liou, C.W. Wang, Hydrogen storage properties of multi-principal-component CoFeMnTi xVyZrz alloys, Int. J. Hydrogen Energy. 35 (2010) 9046–9059. doi:10.1016/j.ijhydene.2010.06.012.

[15] I. Kunce, M. Polanski, J. Bystrzycki, Structure and hydrogen storage properties of a high entropy ZrTiVCrFeNi alloy synthesized using Laser Engineered Net Shaping (LENS), Int. J. Hydrogen Energy. 38 (2013) 12180–12189. doi:10.1016/j.ijhydene.2013.05.071.

[16] I. Kunce, M. Polanski, J. Bystrzycki, Microstructure and hydrogen storage properties of a TiZrNbMoV high entropy alloy synthesized using Laser Engineered Net Shaping (LENS), Int. J. Hydrogen Energy. 39 (2014) 9904–9910. doi:10.1016/j.ijhydene.2014.02.067.

[17] J. Montero, G. Ek, L. Laversenne, V. Nassif, G. Zepon, M. Sahlberg, C. Zlotea, Hydrogen storage properties of the refractory Ti–V–Zr–Nb–Ta multi-principal element alloy, J. Alloys Compd. 835 (2020) 155376. doi:10.1016/j.jallcom.2020.155376.

[18] G. Zepon, D.R. Leiva, R.B. Strozi, A. Bedoch, S.J.A. Figueroa, T.T. Ishikawa, W.J. Botta, Hydrogen-induced phase transition of MgZrTiFe0.5Co0.5Ni0.5 high entropy alloy, Int. J. Hydrogen Energy. 43 (2018) 1702–1708. doi:10.1016/j.ijhydene.2017.11.106.

[19] C. Zlotea, M.A. Sow, G. Ek, J.P. Couzinié, L. Perrière, I. Guillot, J. Bourgon, K.T. Møller, T.R. Jensen, E. Akiba, M. Sahlberg, Hydrogen sorption in TiZrNbHfTa high entropy alloy, J. Alloys Compd. 775 (2019) 667–674. doi:10.1016/j.jallcom.2018.10.108.

[20] J. Montero, C. Zlotea, G. Ek, J. Crivello, L. Laversenne, M. Sahlberg, TiVZrNb Multi-Principal-Element Alloy : Sorption Properties, (2019).

[21] M.M. Nygård, G. Ek, D. Karlsson, M.H. Sørby, M. Sahlberg, B.C. Hauback, Counting electrons - A new approach to tailor the hydrogen sorption properties of high-entropy alloys, Acta Mater. 175 (2019) 121–129. doi:10.1016/j.actamat.2019.06.002.

[22] M.M. Nygård, G. Ek, D. Karlsson, M. Sahlberg, M.H. Sørby, B.C. Hauback, Hydrogen storage in high-entropy alloys with varying degree of local lattice strain, Int. J. Hydrogen Energy. 44 (2019) 29140–29149. doi:10.1016/j.ijhydene.2019.03.223.

[23] C. Zhang, Y. Wu, L. You, X. Cao, Z. Lu, X. Song, Investigation on the activation mechanism of hydrogen absorption in TiZrNbTa high entropy alloy, J. Alloys Compd. 781 (2019) 613–620. doi:10.1016/j.jallcom.2018.12.120.

[24] C. Zhang, A. Song, Y. Yuan, Y. Wu, P. Zhang, Z. Lu, X. Song, Study on the hydrogen storage properties of a TiZrNbTa high entropy alloy, Int. J. Hydrogen Energy. 45 (2020) 5367–5374. doi:10.1016/j.ijhydene.2019.05.214.

[25] P. Edalati, R. Floriano, A. Mohammadi, Y. Li, G. Zepon, H.W. Li, K. Edalati,

Reversible room temperature hydrogen storage in high-entropy alloy TiZrCrMnFeNi, Scr. Mater. 178 (2020) 387–390. doi:10.1016/j.scriptamat.2019.12.009.

[26] J. Hu, H. Shen, M. Jiang, H. Gong, H. Xiao, Z. Liu, G. Sun, X. Zu, A DFT study of hydrogen storage in high-entropy alloy TiZrHfScMo, Nanomaterials. 9 (2019) 1–12. doi:10.3390/nano9030461.

[27] B.H. Toby, R.B. Von Dreele, GSAS-II: the genesis of a modern open-source all purpose crystallography software package, J. Appl. Crystallogr. 46 (2013) 544–549. doi:10.1107/S0021889813003531.

[28] K. Sakaki, H. Kim, K. Asano, Y. Nakamura, Hydrogen storage properties of Nb-based solid solution alloys with a BCC structure, J. Alloys Compd. 820 (2020) 153399. doi:10.1016/j.jallcom.2019.153399.

[29] T. Kazumi, T. Tamura, A. Kamegawa, H. Takamura, M. Okada, Effect of absorption-desorption cycles on structure and stability of protides in Ti-Cr-V alloys, Mater. Trans. 43 (2002) 2748–2752. doi:10.2320/matertrans.43.2748.

[30] M. Aoki, T. Noritake, A. Ito, M. Ishikiriyama, S.I. Towata, Improvement of cyclic durability of Ti-Cr-V alloy by Fe substitution, Int. J. Hydrogen Energy. 36 (2011) 12329–12332. doi:10.1016/j.ijhydene.2011.07.019.

[31] J.O. Abe, A.P.I. Popoola, E. Ajenifuja, O.M. Popoola, Hydrogen energy, economy and storage: Review and recommendation, Int. J. Hydrogen Energy. 44 (2019) 15072–15086. doi:10.1016/j.ijhydene.2019.04.068.

[32] S. Selvaraj, A. Jain, S. Kumar, T. Zhang, S. Isobe, H. Miyaoka, Y. Kojima, T. Ichikawa, Study of cyclic performance of V-Ti-Cr alloys employed for hydrogen compressor, Int. J. Hydrogen Energy. 43 (2018) 2881–2889. doi:10.1016/j.ijhydene.2017.12.159.

[33] T.B. Flanagan, W.A. Oates, Thermodynamics of lntermetallic Compound-Hydrogen Systems, L, Springer-Verlag, 1988.

[34] B.K. Singh, G. Shim, S.W. Cho, Effects of mechanical milling on hydrogen storage properties of Ti0.32 Cr0.43 V0.25 alloy, Int. J. Hydrogen Energy. 32 (2007) 4961–4965. doi:10.1016/j.ijhydene.2007.07.010.

[35] H.C. Lin, K.M. Lin, K.C. Wu, H.H. Hsiung, H.K. Tsai, Cyclic hydrogen absorption-desorption characteristics of TiCrV and Ti0.8 Cr1.2 V alloys, Int. J. Hydrogen Energy. 32 (2007) 4966–4972. doi:10.1016/j.ijhydene.2007.07.057.

[36] L. Hao, C. Yungui, Y. Yigang, W. Chaoling, T. Mingda, Cyclic properties of hydrogen absorption and desorption in V-Ti-Cr-Fe(Al,Si) alloy, Mater. Sci. Eng. A. 448 (2007) 128–134. doi:10.1016/j.msea.2006.10.055.

[37] T. Kabutomori, H. Takeda, Y. Wakisaka, K. Ohnishi, Hydrogen absorption properties of TiCrA (A ≡ V, Mo or other transition metal) B.C.C. solid solution alloys, J. Alloys Compd. 231 (1995) 528–532. doi:10.1016/0925-8388(95)01859-X.

[38] H. Kim, K. Sakaki, Y. Nakamura, Improving the cyclic stability of VTiMn bcc alloys using interstitial elements, Mater. Trans. 55 (2014) 1144–1148. doi:10.2320/matertrans.MG201412.

[39] C.C. Shen, H.C. Li, Cyclic hydrogenation stability of γ-hydrides for Ti25V35Cr40

alloys doped with carbon, J. Alloys Compd. 648 (2015) 534–539. doi:10.1016/j.jallcom.2015.07.021.

[40] A. Kumar, K. Shashikala, S. Banerjee, J. Nuwad, P. Das, C.G.S. Pillai, Effect of cycling on hydrogen storage properties of Ti 2CrV alloy, Int. J. Hydrogen Energy. 37 (2012) 3677–3682. doi:10.1016/j.ijhydene.2011.04.135.